Geophysical Journal International

Geophys. J. Int. (2025) **241,** 1947–1961
Advance Access publication 2025 April 18
GJI Seismology

https://doi.org/10.1093/gji/ggaf142

A controlled-source physical model for long period seismic events

Sananda Ray, Gregory P. Waite and Roohollah Askari

Department of Geological and Mining Engineering and Sciences, Michigan Technological University, 49931, USA. E-mail: raskari@mtu.edu

Accepted 2025 April 16. Received 2025 April 16; in original form 2024 December 22

SUMMARY

Long-period seismic events (LPs) are observed within active volcanoes, hydrothermal systems and hydraulic fracturing. The prevailing model for LP seismic events suggests that they result from pressure disturbances in fluid-filled cracks that generate slow, dispersive waves known as Krauklis waves. These waves oscillate within the crack, causing it to act as a seismic resonator whose far-field radiations are known as LP events. Since these events are generated from fluid-filled cracks, they have been used to analyse fluid transport and fracturing in geological settings. Additionally, they are deemed precursors to volcanic eruptions. However, other mechanisms have been proposed to explain LP seismicity. Thus, a robust interpretation of these events requires understanding all parameters contributing to LP seismicity. To achieve this, for the first time, we have developed a physical model to investigate LP seismicity under controlled-source conditions. The physical model consists of a 30 cm × 15 cm × 0.2 cm crack embedded within a concrete slab with dimensions of 3 m × 3 m × 0.24 m. Using this apparatus, we investigate fundamental factors affecting long-period seismic signals, including crack stiffness, fluid density and viscosity, radiation patterns and triggering location. Our findings are consistent with the theoretical model for Krauklis waves within a fluid-filled crack. In this study, we examine the interplay between fluid properties and characteristics of waves within and radiated from the crack model. Records from a pressure transducer within the crack model have the same frequency characteristics as the surface sensors, indicating that the surface sensors are recording the crack waves. Because the crack stiffness parameters for all the fluids are relatively high, fluid density variations have a larger effect on the crack wave frequency, with higher density fluids yielding lower resonance frequencies. Similarly, the quality factor (Q) decreases with increasing fluid density. We also find that an increase in fluid viscosity along with the increased fluid density results in a decrease in resonance frequency and Q. Trigger locations at the middle of the crack length and width most effectively resonated the first and second transverse modes. Thus, this physical model can offer new horizons in understanding LP seismicity and bridge the gap between theoretical models and observed LP signals.

Key words: Fourier analysis; Controlled source seismology; Volcano Seismology; Wave propagation..

1. INTRODUCTION

The study of volcanic seismic signals plays an important role in the characterization of fluid dynamics in terms of the physical process beneath the Earth. In addition to the usual brittle crack-related earthquake signals (volcano-tectonic, or VT, earthquakes), seismic signals on volcanoes include long-period events (LPs), very-long-period events (VLPs), and tremor-like signals (Chouet & Matoza 2013). Unlike VTs, LPs, VLPs and tremors are usually related to fluid-filled cracks. In particular, LPs and some types of tremors can be linked to a resonating fluid-filled conduit, driven by a pressure disturbance in the magmatic or hydrothermal system (Chouet 1996). Long period seismograms usually have a strong high-frequency signal at the onset followed by a decaying harmonic oscillation with a period of 0.2–2 s (Chouet 1996; Nakano *et al.* 1998; Kumagai & Chouet 1999, 2001). In volcanic settings, LPs can be associated with magma degassing. The presence of bubbles and hydrothermal fluids will lower the sound speed in magma inducing a sharp velocity contrast, which creates a favourable condition for the entrapment of the acoustic energy. However, when the crack stiffness is significantly greater than one, as observed in experiments (Cao *et al.* 2020, 2021; Ray *et al.* 2024), generation of LPs predominantly involve nearly incompressible fluid motion. With elastic crack opening and closing serving as the restoring force for wave propagation, the dynamics

of these waves differ from the trapping of acoustic energy in the fluid. Instead of being driven by the entrapment of acoustic energy, these waves primarily involve the fluid's motion, with negligible energy stored in fluid compression (Dunhum & Ogden 2012). In a hydrothermal system, the LP excitation mechanism happens due to the heat transfer from the underlying magma body, which increases the pressure inside the steam-filled crack leading to the opening and collapsing of the crack (Kumagai *et al.* 2002, 2005; Nakano *et al.* 2003; Waite *et al.* 2008; Matoza *et al.* 2009). LP events and tremors share many characteristics; however, tremors have longer durations and may be explained by sustained excitation of sources (Syahbana *et al.* 2014).

LP seismicity has been observed at many volcanoes including Kusatsu–Shirane, Japan (Fujita *et al.* 1995; Nakano *et al.* 1998; Kumagai *et al.* 2002; Nakano & Kumagai 2005), Asama, Japan (Aoyama & Takeo 2001; Fujita & Ida 2003), Galeras, Colombia (Gil Cruz & Chouet 1997), Tungurahua, Ecuador (Molina *et al.* 2005), and Papandayan, Indonesia (Syahbana *et al.* 2014) and can dominate during fluid transport, thus serving as an important eruption precursor. As the properties of the LP events crucially depend on the fluids involved, these can be used in the characterization of the fluid type, its scale of transport, and other magmatic processes like magma de-gassing or intrusion. For instance, crack growth and collapse in a hydrothermal system of Kusatsu–Shirane volcano, Japan was interpreted by Kumagai *et al.* (2002) using the temporal changes in frequency and quality factor of the LP events. LP events at Kusatsu–Shirane were modelled as cracks filled with misty gas by Kumagai *et al.* (2002) and Taguchi *et al.* (2018, 2021).

The first quantitative modelling of the LP and tremor signals was done by Aki *et al.* (1977) from volcanic tremors at Kilauea, Hawaii, where the sudden opening or extension of a magma-filled crack (tensile crack model) was assumed to be the reason behind the LP signals, but the fluid motion concerning the conduit wall was neglected. Later, the active participation of fluid was included, and the model was modified using a fluid-filled rectangular crack, by Chouet (1986, 1988) and Chouet & Julian (1985). Chouet (1986, 1988) demonstrated numerically that a pressure disturbance on the crack initiates a slow dispersive wave called the crack wave [also 'Krauklis' wave (Krauklis 1962; Korneev 2008)] that propagates slower than the acoustic velocity of the fluid in the crack, whose far-field radiations are recorded as LP events in volcanic and hydrothermal setting. The slow speed of the Krauklis wave allows us to characterize the frequency of the LP events using the resonance property without the need for an unrealistically large magma reservoir (Ferrazzini & Aki 1987). Chouet (1986) introduced two dimensionless parameters that are called crack stiffness (C) and viscous damping (F) written as:

$$C = \frac{b}{\mu}\frac{L}{d}, \tag{1}$$

$$F = \frac{12\eta L}{\rho_f d^2 \alpha}, \tag{2}$$

where b is the fluid bulk modulus, μ is the matrix rigidity, L length of the crack, d crack aperture, η fluid viscosity, ρ_f fluid density and α is the P- wave velocity in the solid.

Later, Chouet (1988) explained the far-field radiation properties in terms of crack stiffness, fluid viscosity, trigger position and trigger area. His seminal work, which we hereafter refer to as Chouet's model, demonstrates that increasing crack stiffness produces a shift of the spectral peak toward lower frequency and decreases the bandwidth, amplitude and spacing between the peaks. In addition, fluid viscosity smears out the high-frequency peaks of the spectrum and decreases the amplitude of the dominant and subdominant peaks. Chouet (1988) also demonstrated that the resonance frequencies of the far-field radiation of crack waves (commonly referred to as LP seismic events) are primarily dependent on the property of the crack itself and are independent of all distance and azimuths.

Chouet's model has been thoroughly explored numerically, however it has not been quantitatively tested by laboratory experiments. State-of-the-art studies on the physical modelling of LP events (e.g. Burlini *et al.* 2007; Benson *et al.* 2014; Derode *et al.* 2015; Fazio *et al.* 2017; Namiki *et al.* 2019) have been focused on explaining the mechanism of the LP events rather than quantitative analysis concerning the crack stiffness, fluid viscosity and dynamics, and other fluid and crack properties.

Additionally, although the general framework to explain LP seismicity is based on pressure disturbances in fluid-filled cracks, other theories have also been presented. Bean *et al.* (2014) showed that the gradual failure of tensile cracks in dry rocks can create signals highly similar to some LP signals. In such cases, the occurrence of LP events cannot necessarily be associated with fluid transport and dynamics. James *et al.* (2016) and Corona-Romero *et al.* (2012) also demonstrated that mass transport in conduits can generate LP signals. Thus, a robust interpretation of LP events requires an understanding of all parameters contributing to LP seismicity.

In this study, for the first time, we developed a controlled-source physical model to extensively investigate all fundamental parameters impacting LP events, including crack stiffness, fluid viscosity, triggering location and radiation pattern. Our physical model consists of a concrete slab with dimensions of 3 m × 3 m × 0.24 m, in which a 30 cm × 15 cm × 0.2 cm horizontal crack is embedded. A piezoelectric source was used to induce pressure disturbances within the crack. Several accelerometers and one pressure transducer were employed to record emitted signals.

Since analytical and numerical modelling necessitates some degree of simplification, physical modelling is advantageous in terms of considering more realistic conditions, present in natural settings. Thus, our approach will allow for studying LP seismicity under various realistic conditions to enhance our interpretation and analysis.

2. PHYSICAL MODEL

2.1 Setup preparation

We have built our physical model using concrete because it has properties similar to natural rock types. Our physical model involves a 30 cm ×15 cm × 0.2 cm crack, embedded with a small slab that in turn is enclosed within another large concrete slab model with dimensions of 3 m × 3 m × 0.24 m (illustrated in Fig. 1b). Vertical channels were connected to the buried horizontal crack model inside the concrete slab to induce pressure waves using a piezo-electric source and to record the Krauklis wave using a piezo-electric pressure transducer receiver. The existence of these small vertical channels may alter the seismic signals slightly but should not prevent a comparison with simple rectangular crack models.

We cast the large concrete slab over a layer of absorbing foam with a thickness of 10 cm. The foam layer serves three functions: (1) absorbing signals impinging on the bottom of the slab, (2) isolating the concrete from ambient vibrations, and (3) thermally insulating the slab to prevent cracking within the slab. In the centre of the slab, we left a cavity measuring 40 cm x 40 cm x 22 cm to accommodate the smaller concrete slab, which was installed later. The major consideration in this setup was to avoid recording signals reflected

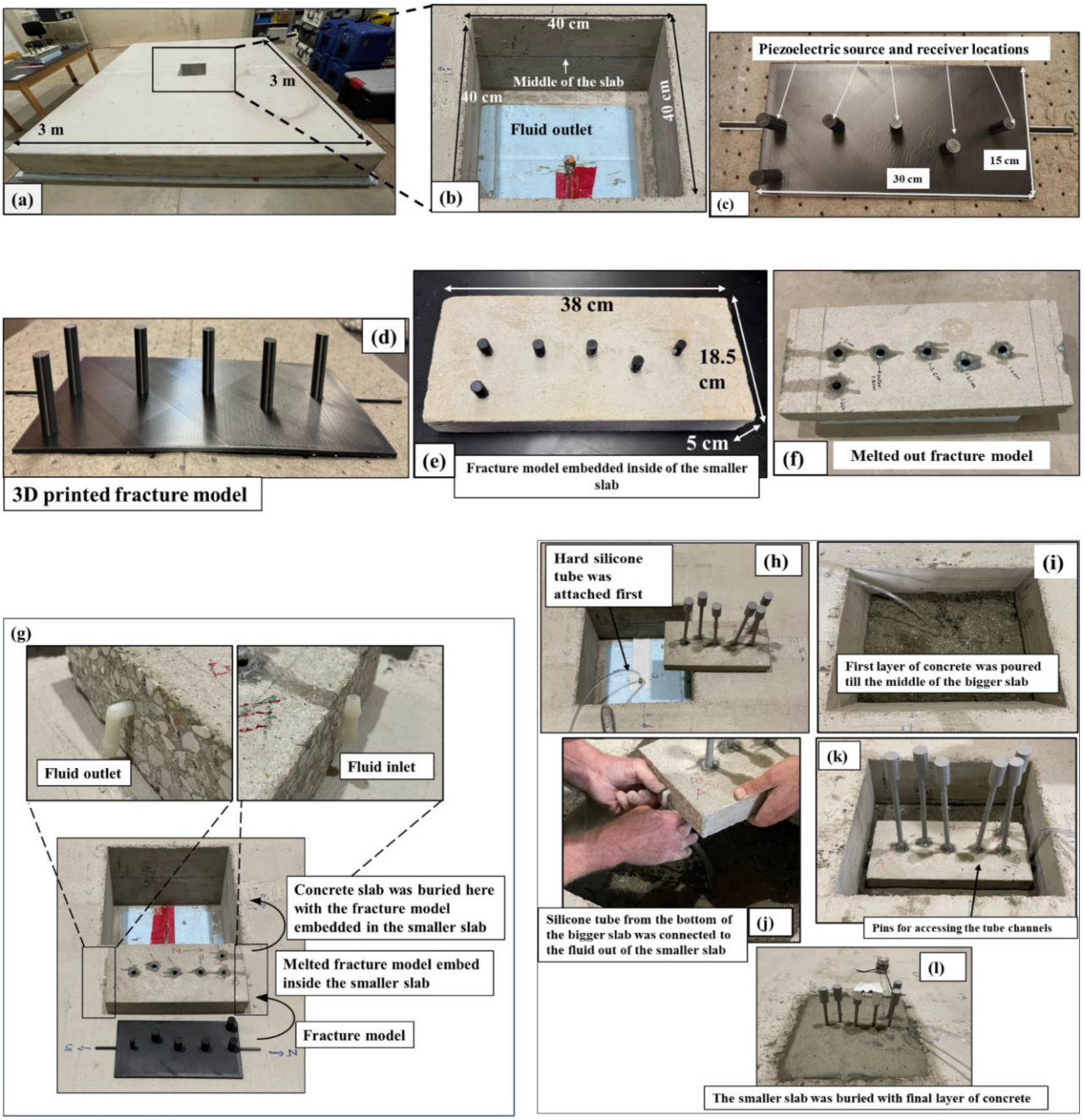

Figure 1. The bigger concrete slab (a) and the rectangular excavated part in the middle of it (b). The 3-D printed crack model is shown in panels (c) & (d). The embedded crack model inside the smaller slab (e) and the slab after melting out the crack model (f). Visualization of the fluid inlet and outlet with respect to the smaller slab (g). Step-by-step photos showing the attachment of the smaller concrete slab with the crack model to the bigger concrete slab. Excavated part within the larger slab, hard silicone tubes were used to attach the fluid channels inside the bigger slab with the smaller one (h). A layer of concrete was poured into the middle of the empty section (i). The smaller concrete slab was kept on top of the poured concrete after making sure that the freshly poured concrete had cured enough to avoid the problem of the smaller slab sinking (j and k). (l) 3-D printed pins were used to ensure that we had access to the void or crack after burring the crack model completely, which were removed later.

from the sides of the slab. Thus, we opted for such a large width and length (3 m x 3 m) to attenuate side reflections through geometrical spreading and intrinsic absorption.

To create a crack within the concrete slab, we first 3-D printed a solid pattern with dimensions of 30 cm x 15 cm x 0.2 cm (the crack model dimensions, Fig. 1d). The pattern was made from industrial wax with a low melting point of 70 °C. As shown in Fig. 1(d), the rectangular pattern includes cylinder-like structures that serve as conduits for source and fluid transport (Fig. 2). Next, the wax pattern was placed inside an aluminum mold with dimensions of 38 cm × 18.5 cm × 5 cm. It was then filled with a homogeneous concrete mixture, using the same composition used for the large slab. During this stage, we ensured no gas pockets were trapped during casting. After the concrete was cured, the slab was placed in an oven to slowly melt and drain the wax, leaving the desired crack-shaped void. Thus, we created a small concrete slab with an

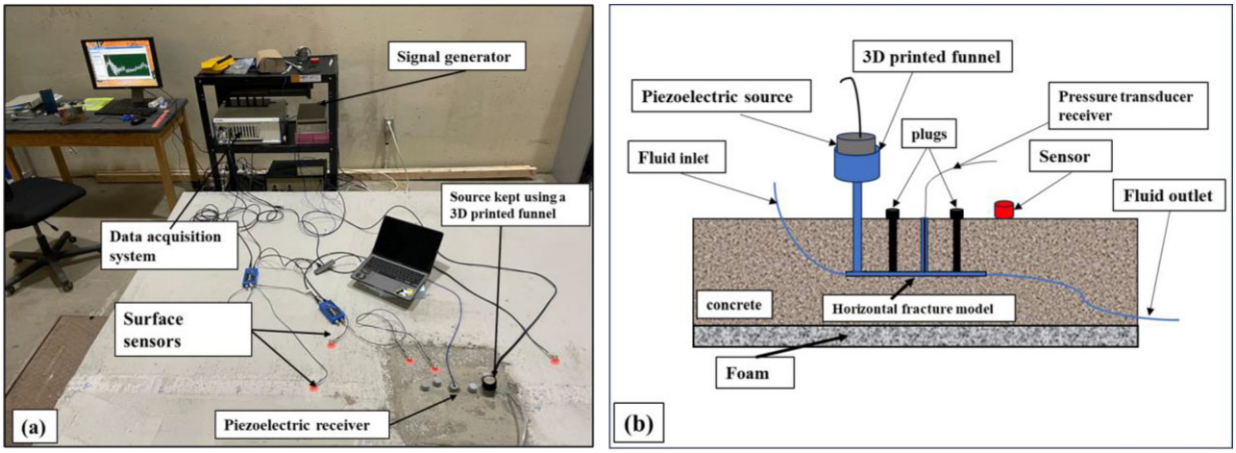

Figure 2. (a) General experimental set-up in the lab. (b) Source configuration with respect to the concrete slab and the crack model.

embedded crack. This small slab was then placed within the hole centred in the large concrete slab and was connected to the fluid inlet and outlet pipes that had been positioned during the casting of the large slab. These pipes facilitated fluid injection and extraction during experiments. Finally, while the small slab was positioned in the middle of the hole (11 cm from its bottom or 11 cm from its surface), it was filled with the same concrete to create a nearly uniform overall slab with an embedded crack at its centre. The step-by-step process of attaching the smaller concrete slab to the larger one can been referenced to the Figs 1(h)–(l).

Fig. 2(a) shows a schematic cross-sectional view of the data acquisition, and Fig. 2(b) shows an actual configuration of data acquisition with respect to the surface sensors. The source is placed outside of the crack within a funnel, and its pulse is transmitted to the crack through one of the conduits. In another conduit, the pressure transducer is placed, while the other conduits have been plugged. Both the funnel and the conduit are filled with the same crack fluid. Thus, when the source is excited, the pressure pulse is transferred into the crack through the funnel and conduit.

2.2 Crack model aperture

Before embedding the smaller concrete slab inside the larger one, we wanted to ensure that we would acquire strong signals within the frequency range from 0 to 10 kHz. Based on our initial assessments from theoretical models, we concluded that a crack with an aperture ranging from 2 to 6 mm would produce LP signals within this frequency range. Therefore, we built two small slabs with embedded cracks, with apertures of 2 and 6 mm, respectively. Similar to Cao *et al.* (2021), we placed the small slabs within a pool of water. We used a pressure transducer inside the cracks to record the Krauklis waves initiated within them. This initial investigation revealed that the crack with a 2 mm aperture produced the strongest Krauklis wave signals. Thus, we decided to embed the slab with the 2 mm crack into the large slab and also used a source frequency of 3000 Hz for our subsequent experiments.

2.3 Data acquisition system

To initiate pressure disturbances within the crack, we utilized a piezoelectric transducer (OLYMPUS X1021) with a resonant frequency of 50 kHz. Using an arbitrary waveform generator, a tone-burst sine wave was generated at 3 kHz with an amplitude of 5 V. By placing one of the piezoelectric pressure transducers against the source surface, the source signature was captured (the source signature and its amplitude spectrum can be observed in Fig. S7, Supporting Information). The source was positioned within a funnel that is connected to the crack through a conduit (Fig. 2). To generate the pressure pulse, we used a signal generator (DS345 model from Stanford Research Systems). The signal produced by the generator was amplified with a signal amplifier (Krohn-Hite 7500) and conditioned using a PCB Piezotronics 482C signal conditioner. The data acquisition system is a PXI-5922 high-resolution oscilloscope with a minimum sampling rate of 50 ksps.

To record LP events, we used five accelerometers (R3A model from Physical Acoustics) which have a flat response from 0 Hz to 20 kHz, ideal for recording our data given the frequency range we used in our experiments. Additionally, we placed a pressure transducer (PCB Model 152 113B21) close to the crack wall to record the Krauklis waves propagating within the crack. The pressure transducer has a low-frequency response of 0.5 Hz, a sensitivity of 100 mV/kPa, and a resonant frequency of 500 kHz. Thus, through the data recorded by the pressure transducer and accelerometers, we can compare the Krauklis waves within the crack to LP event signals on the slab's surface.

2.3 Stiffness

To determine the P wave velocity in the concrete slab, we positioned five accelerometers at a 10 cm interval on top of the concrete slab and used the same piezo-electric source. The seismic data acquired from the accelerometers were dominated by strong Rayleigh waves. The arrival times of Rayleigh waves were manually picked and were plotted against the offset distances. A linear regression line was then fitted into data points, and an inverse of a slope of the line yielded the velocity of Rayleigh waves in concrete. Through the analysis of the Rayleigh wave (the velocity of Rayleigh waves is approximately 57 per cent that of the primary waves for a normal strength concrete (Aggelis 2011) we estimated the P wave velocity to be 3824 m s^{-1}. Considering the Poisson's ratio of the concrete to be 0.2, the S wave velocity will be 2342 m s^{-1}. To determine the density of the concrete slab we used, we cut a small cubic piece from the slab and measured the volume and the weight of the cube, which gave us the density as 2627 kg m^{-3}. Considering the bulk modulus of water as 2.15 GPa, our initial crack model incorporating water as a fluid, exhibits a crack stiffness of 22.8 (using eq. 1).

3. DATA PROCESSING

Two important aspects of LP signals are their resonance frequencies and quality factors. To enhance estimates of these two properties, we improved our data quality by stacking and applying a band-pass filter to our data. These two approaches significantly reduced the ambient noise that was prevalent in the lab environment. To choose appropriate frequencies for the band-pass filter, we analysed the ambient noise within the experimental room to enable the filtration of extraneous noisy data from our experimental observations. Unfortunately, a strong background noise due to other lab equipment was prevalent with a frequency ranging from 0 to about 1000 Hz. Thus, the lowest end of the bandpass filter was 1000 Hz to remove the background noise. The amplitude spectrum of the background noise can be seen in Fig. S5 (Supporting Information).

For the spectral analysis, we applied the Fast Fourier Transform followed by the normalization of the amplitude spectrum. While many studies have used the Sompi method to estimate quality factors (Hori *et al.* 1989; Kumazawa *et al.* 1990; Kumagai & Chouet 2000; Tary *et al.*, 2014), we find that complications in the signal described below affect the decaying coda and result in artificially high-quality factors. Instead, we employ a method in which the quality factor (Q) is determined from the shape of the spectral peak (Bourbie *et al.* 1987). We fit the observed spectra with a Lorentzian using the Nelder–Mead simplex direct search method (Bourbie *et al.* 1987; Haney *et al.* 2021). The function can be written as:

$$P(f, A, f_1, w) = \frac{Aw^2}{4(f - f_1)^2 + w^2}, \tag{3}$$

where, P is the modelled power spectrum as a function of frequency and three fitting parameter A (peak amplitude), f_1 (resonance frequency) and w (with of the spectrum at the half peak value). After fitting the observed spectra, these three parameter estimates are obtained and from that the Q value is calculated using $Q = f_1/w$ (Bourbie *et al.* 1987). The fitted spectra and associated Q values are shown below. If we compare the Q values for the modes represented in the Fig. 5 above, the $2L/5$ longitudinal mode has a higher Q value (less attenuation) in case of the one fourth trigger location.

4. EXPERIMENTAL OBSERVATIONS

Our experiments explored four aspects of the Chouet's model that have previously been investigated theoretically and/or numerically: trigger location, radiation pattern, crack stiffness and fluid viscosity. The experiments are described in that order below. We mainly focus on our experimental observations after embedding the smaller concrete slab within the large slab.

4.1 Trigger location

Crack waves, or Krauklis waves, are typically described as standing waves that form within a crack, with displacement patterns determined by the interaction of compressional and shear stresses at the crack faces. The modes of crack waves are classified into three main categories: longitudinal, transverse and mixed. The longitunal mode describes wave propagation along the crack length. The transverse mode describes wave propagation along the width of the crack. The mixed mode, involves a combination of both longitudinal and transverse modes, leading to a more complex wave pattern. These standing wave modes exhibit distinct oscillation patterns that reflect the unique interaction of forces within the crack. As the far field radiation of the crack wave is also known as the long period seismic wave or LP events, the modes generated by the crack waves are used to demonstrate the resonance frequencies observed in the field. As there is no mass movement inside the crack model, the fundamental frequency is counted from mode $m = 2$.

Previous work describes the effect of trigger location on resonant mode excitation. According to Chouet's model, a trigger at the one-fourth of the crack length and across the entire width can best excite the fundamental resonant frequency. Taguchi *et al.* (2021) observed that a trigger at the centre of the crack model spread across a narrow strip through the entire width, effectively excites the odd longitudinal modes, specifically third & fifth modes and the associated frequency (lowest observable frequency).

The layout of this experiment can be referenced to Fig. 3(g), where the numbers 1–6 are represented as the possible trigger locations. Specifically, locations 1–4 have been named as edge 1, edge 2, one-fourth and middle for the rest of the experiment. The trigger locations in terms of the length and width of the crack model have also been described in Fig. 3(g). One thing to note about the trigger locations in this experiment is that the trigger locations have a diameter of 0.6 cm, which is about 4 per cent the crack width and the middle position is located at the centre of the rectangular crack model. Surface sensors were kept according to the layout, where the distance of the sensors from the crack model has shown in the Fig. 3(g). This layout was used to optimize the best possible sensor locations for high signal-to-noise ratio data along with the symmetrical layout of the crack model concerning the bigger concrete slab. As our trigger point was not spread across the entire width of the crack model, we expect to observe both the longitudinal mode and transverse modes along with the complex modes. The comparison of waveforms between the crack wave (obtained from the pressure transducer) and its radiation (recorded at the surface sensors) is presented in Figs 3(b)–(f). Our observations indicated that, the response of the crack wave away from the crack model is dependent on the sensor locations, as the contact between the smaller slab bearing the crack model and the bigger slab was not uniform surrounding the smaller slab, where we need to consider the fluid inlet and outlets connected to the slab resulting in small discontinuity between the two slabs.

During the recording of the crack wave response, we also observed reflected tube waves, which arrived approximately 5 and 13 milliseconds after the onset of primary crack waves. These tube waves are marked with a red arrow in Fig. 3(a) and can be seen in both the crack wave and its response. We calculated the velocity of the tube waves travelling through the silicone-vinyl tubes used in the experiments to be 299 m s^{-1}. The first wave came from the 72 cm tube used to inject fluid into the crack, while the second originated from a 2 m tube in the outlet, used to drain fluid. The arrival times of the tube waves align with our experimental data, considering the lengths of the tubes emerging from the slab and those routed beneath it for fluid injection. The difference in polarity is due to the open versus closed conditions of the two tube ends. More detailed calculations supporting these findings can be found in Appendix A below. For most stations, the secondary arrival coincides with the arrival of the tube waves.

We also present the comparison between the frequency spectrum obtained by pressure transducer and the surface sensors in Figs 4(a)–(d) below. As observed from Fig. 4, we can see that data obtained from the pressure transducer and the surface sensors share similar

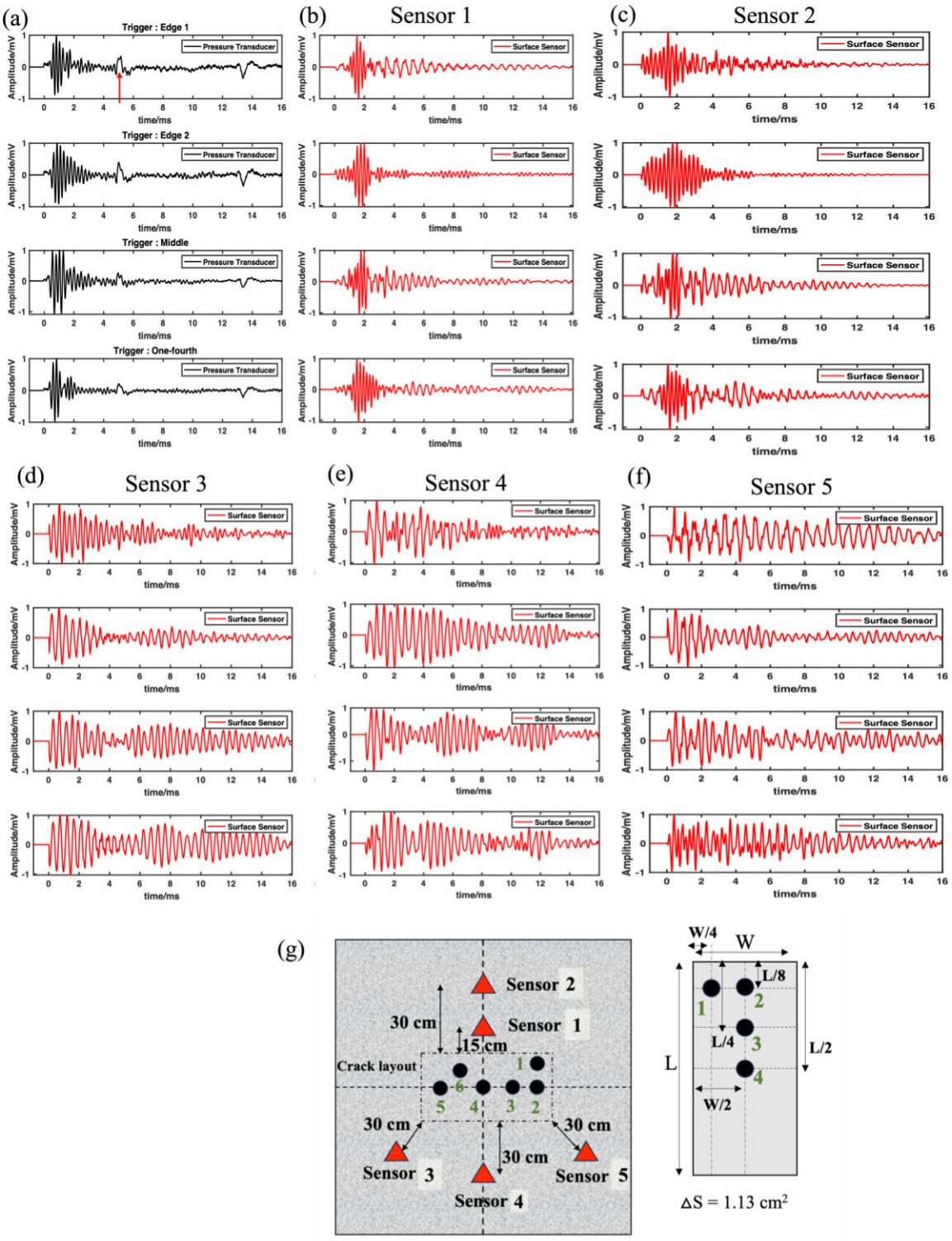

Figure 3. (a) Waveforms collected using a pressure transducer at the fifth position. (b)–(f) Waveforms obtained from the surface sensors, where the four panel on the top of each other defines the trigger locations as edge 1, edge 2, middle and one-fourth respectively. (g) Layout used in this experiment.

frequency peaks. According to Kumagai *et al.* (2002), a trigger location exactly at the middle of the crack model will excite the transverse mode with a wavelength of *2 W/3*. The theoretical frequency values and mean values for different trigger locations for different sensor positions are listed in the Table 1 in the Section 4. Fig. 5 illustrates that the trigger locations at edge 2 and one-fourth are effective in exciting the longitudinal modes corresponding to the wavelengths *2 L/3*, *L/2* and *2 L/5*, while the middle trigger location efficiently resonates the transverse modes. In contrast, the first mixed mode, which also dominates at the sensor 3 location, is observable when the trigger is placed at edge 1. The observed modes for different trigger locations at sensor location 1 are displayed in Fig. 5 and the observed Q values are shown in Fig. 6. Notably, the dominant frequency observed for the middle trigger location corresponds to

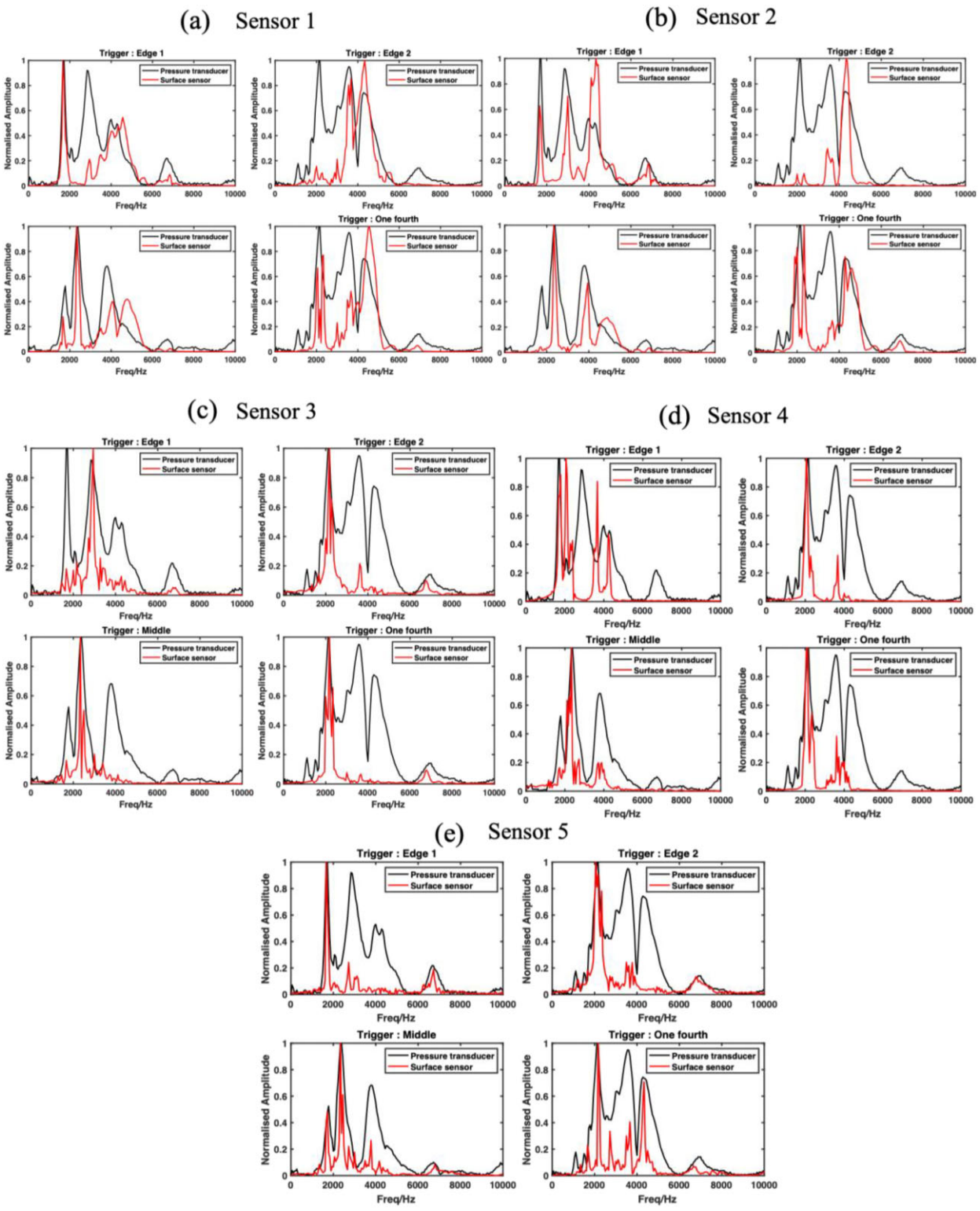

Figure 4. (a)–(e) The comparison between the frequency spectrum obtained from the pressure transducer and the surface sensor for different trigger location using the layout mentioned in the figure above.

the first transverse wavelength W, with the second prominent peak aligning with the transverse wavelength of $2\,W/3$. According to Cao *et al.* (2021), mode excitation is highly influenced by the source frequency used during the experiment. Given that the source frequency in our experiment is 3000 Hz, it is improbable for the transverse mode corresponding to the 2 W/3 wavelength to emerge as the dominant frequency. One thing is notable, the higher modes are highly attenuated for the sensor locations which are kept at a 30 cm distance.

Table 2 shows the comparison of the mean observable experimental values obtained for different sensor locations with the theoretical values.

Table 1. *Q* factor values associated with the dominant frequencies for different sensor location.

Sensor	*Edge 1*	*Edge 2* *Frequency = 2166 Hz*	*Middle* *Frequency = 2333 Hz*	*One fourth* *Frequency = 2166 Hz*
Sensor 1	20.2	24.1	24.1	17.8
Sensor 2	16.5	16.4	21.6	17.4
Sensor 3	13.8	16	21	13.64
Sensor 4	8.6	12.3	11.8	–

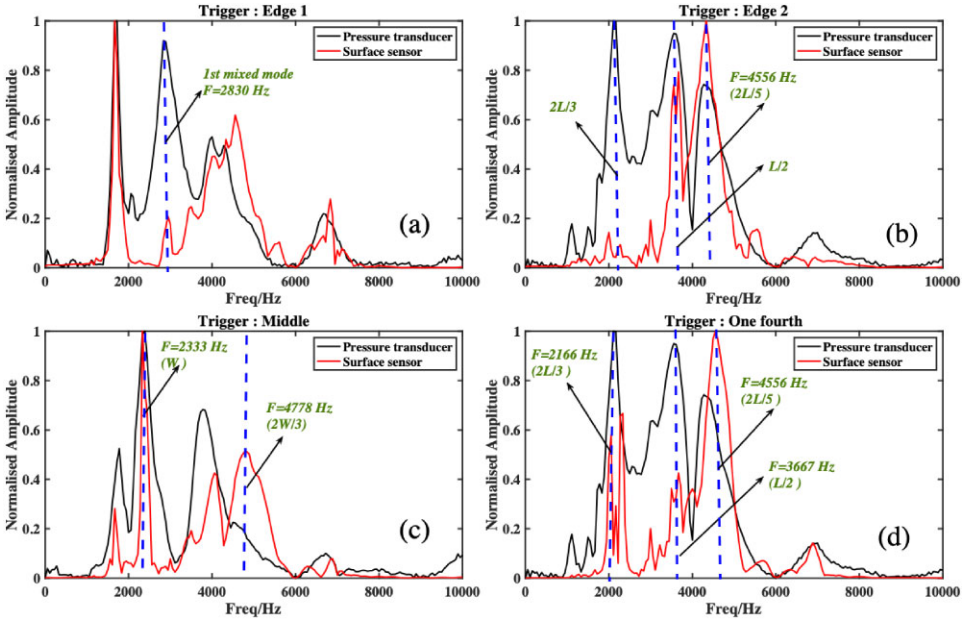

Figure 5. Mode identification for different trigger rate locations where (a), (b), (c) and (d) represent the edge 1, edge 2, middle and one-fourth trigger locations, respectively, for the Sensor 1.

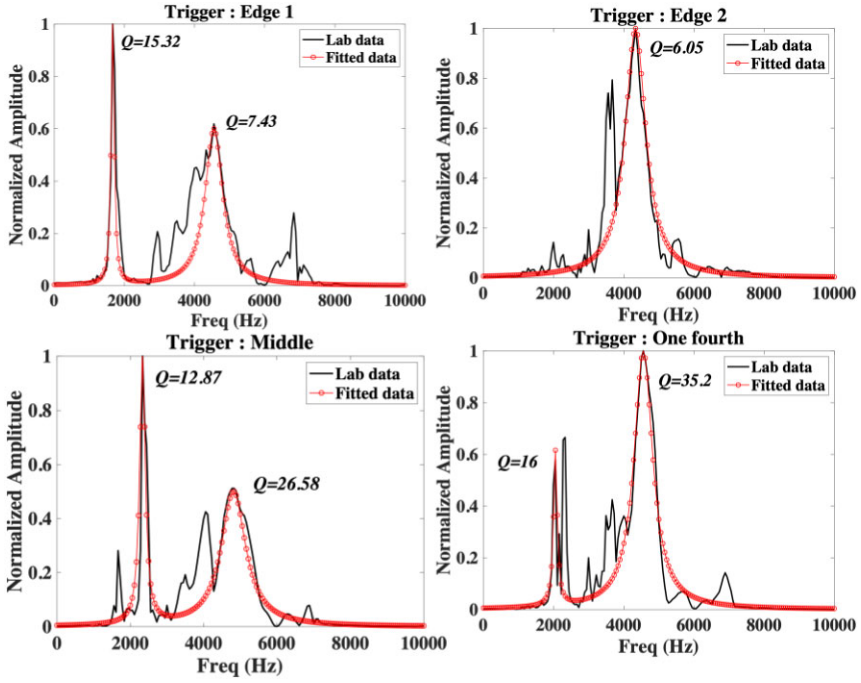

Figure 6. Normalized spectra plotted along with the best fitting Lorentzian function for the Sensors 1, where (a)–(d) represent the Q factor calculation for the trigger locations of edge 1, edge 2, middle and one fourth.

Table 2. Comparison between the theoretical longitudinal frequencies and the observed longitudinal frequency values and the percentage mismatch between them mentioned inside the parenthesis.

Mode number (Wavelength for longitudinal and transverse frequency)	ε_m^L	ε_m^W	*Theoretical frequency (Hz)*		*Observed longitudinal, transverse and mixed frequency values (Hz)*		
			Longitudinal	*Transverse*	*Longitudinal*	*Transverse*	*Mixed*
2 (*L*), (*W*)	0.117	0.0772	1097	2349	–	2333 (0.6 per cent)	2830
3 (2 *L*/3), (2 *W*/3)	0.089	0.0528	2213	5412	2166 (2.1 per cent)	4778 (11 per cent)	–
4 (*L*/2), (*W*/2)	0.071	0.0401	3602	8910	3667 (2 per cent)	–	–
5 (2 *L*/5), (2 *W*/3)	0.058	0.0324	5142	12 705	4556 (11 per cent)	–	–

4.2 Radiation pattern

Using a source frequency of 3000 Hz, we obtained data by placing four surface sensors in a single line with a distinct layout (layout illustrated in Fig. 7e) with variable trigger positions (two different corners of the crack, middle and one-fourth length of the horizontal crack model). There were 15 cm between the surface sensors. To check for differences in data quality and potential discontinuities across the boundary (since the two concretes for the smaller and bigger slab were poured at different times), we placed one sensor inside the boundary of the smaller and bigger concrete slabs in these layouts. The waveforms obtained during this experiment are presented in Fig. S1 (Supporting Information). The amplitude spectra derived from the data are displayed in Fig. 7 below. It is evident that the sensors exhibit similar amplitude spectra for the same trigger location, which reflects the response of the crack resonance. Additionally, Fig. S2 (Supporting Information) shows a comparison of the amplitude spectra between the sensors placed on the surface of the concrete slab and the pressure transducer. Fig. S1 (Supporting Information) shows that for all trigger locations, the fourth sensor (located 45 cm from the crack model) exhibits waveform distortion (indicating that the decaying characteristic typical of a long-period wave is absent). We could not obtain clear results at the Sensor 4 location for the one fourth trigger location.

As described above, the Nelder–Mead simplex method was used to fit the spectra and compute the Q factor related to the observed spectra in Fig. 7 above as well. The Q values corresponding to the dominant frequency, determined through best-fitting curves, are presented in Table 1 below and fitted spectra are presented in Fig. S3 (Supporting Information). From, Table 1, we can observe that we the increasing distance, the Q factor value started decreasing, which indicates higher attenuation at the larger distances.

4.3 Crack stiffness

The purpose of this experiment is to examine the impact of the crack's altered stiffness. Eq. (1) can be utilized to compute crack stiffness. The setup of this experiment was similar to that seen in Fig. 7(e). It is possible to modify stiffness by physically adjusting the crack's length or aperture, but it is also possible to vary stiffness by employing a fluid whose bulk modulus is different. The first experiments used water, which has a bulk modulus of 2.15 GPa and gives a crack stiffness of 22.4. We then employed ethanol, which has a bulk modulus of 1.06 GPa, yielding a crack stiffness of 11.04. It has been explained before (Chouet 1988; Cao *et al.* 2021) that resonance frequency increases as crack stiffness decreases. However, as the value of the crack stiffness in our experiments is much higher than one (C>>1), the change in crack stiffness due to the change in bulk modulus will have little effect on the resonance frequency (Maeda & Kumagai 2013; Lipovsky & Dunham 2015). Rather than bulk modulus or sound speed of the fluid influencing the frequencies, the varying the fluid density becomes important for influencing the frequencies (see Appendix B). Given that water has a density of 1000 kg m^{-3} and ethanol has a density of 789 kg m^{-3} (less than water), which will contribute towards higher resonance frequency of the crack model and the change in frequency should be around 6.8 per cent (the relationship between the fluid density and crack wave resonance is stated in Appendix B). From our experimental results, we could observe an increase of 7 per cent (edge 2 trigger) and 16 per cent increase of frequency (middle trigger). Fig. 8 displays the amplitude spectrum and Q factors that was produced for this experiment. Here, we used the trigger locations in the middle and at the edge of the crack length, as these locations exhibited better signal-to-noise ratio data. The ethanol fluid has generated dominant high-frequency patterns for both trigger locations.

The Q factor has been calculated as well (shown in Fig. S4 in the Supporting Information). We have noted a decrease in the Q factor in case of the trigger location middle and Q factor increases in case of the trigger location at the edge of the crack with respect to water (water has a viscosity of 1 cP and ethanol has a viscosity of 1.2 cP). Now, ethanol still has slightly higher viscosity than water, which might have caused higher viscous drag, eventually lowering the values of the Q factor, in case of the middle trigger location which is also notable in the first sensor for the edge trigger.

4.4 Viscosity

Finally, we examined the effect of different fluid viscosity on the radiated spectra. Viscous damping (eq. 2) attenuates the higher frequencies more rapidly, as demonstrated by Chouet (1988). We employed the experimental configuration depicted in Fig. 7(e) and switched from water to polyethylene glycol (PEG) solution for this experiment, with a molecular weight of 8000 g mol^{-1}. By dissolving 1200 g of polyethylene glycol in 5 L of water at room temperature, we obtained a solution with a density of 1240 kg m^{-3}. Water has a viscosity of 1 cP and the PEG solution used in our experiment exhibits a viscosity value of 11.1 cP (measured using a viscometer). The amplitude spectrum along with the quality factor analysis is shown in the Fig. 9. As we can see the PEG solution has generated lower-frequency dominant peaks. As previously noted, fluid density plays a key role in explaining resonance frequency behaviour. Because the PEG solution is denser than water, it may shift the resonance toward lower frequencies (Appendix B). For this experiment, we employed the middle trigger position based on the previous observation for stiffness, radiation pattern and trigger location effects, with the sensor locations maintained at 1 and 2, as shown in Fig. 7(e). We can note that Q decreases with the viscous fluid.

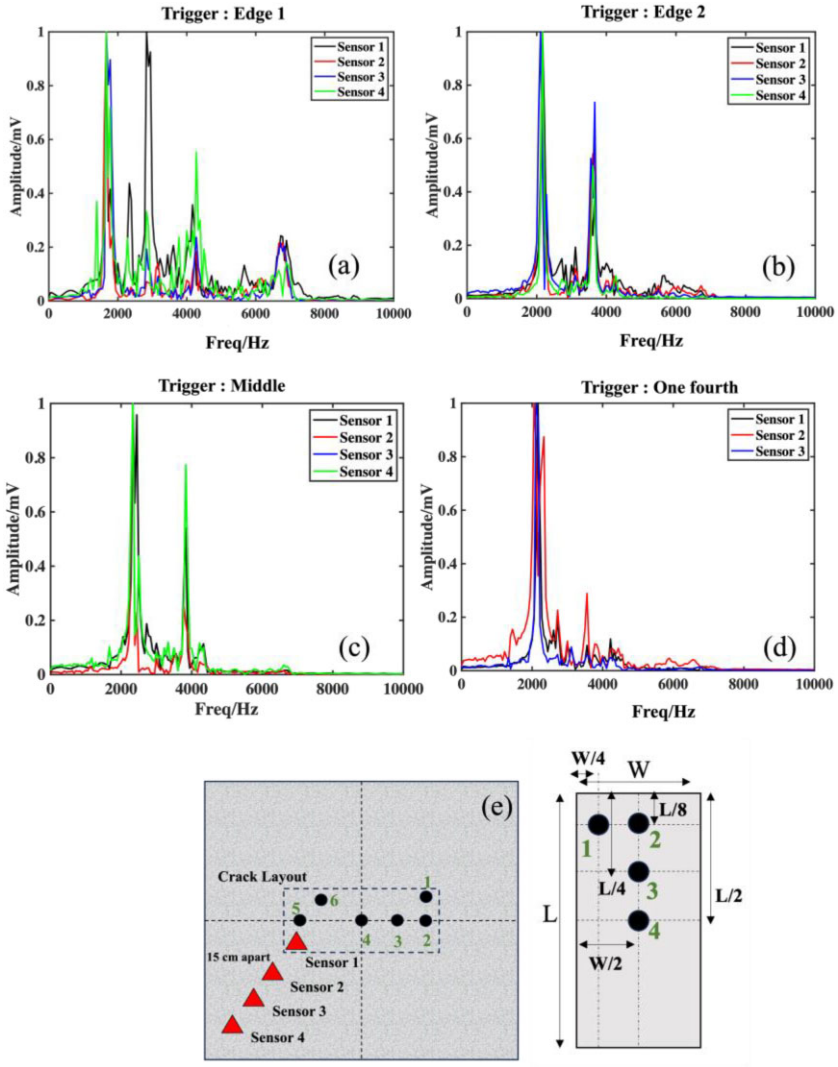

Figure 7. (a)–(d) The comparison between the normalized frequency spectra due to different receiver locations for fixed trigger locations, such as edge 1, edge 2, middle, and one-fourth of the crack length. (e) The layout of the experiment.

5. DISCUSSION

5.1 Comparison between observations and theory

For a rectangular crack, the theoretical longitudinal and transverse modes of an LP event can be obtained by (Maeda & Kumagai 2013)

$$f_m^L = \frac{(m-1)\,a}{2L\sqrt{1+2\varepsilon_m^L c}}, \tag{4}$$

$$f_m^W = \frac{(m-1)\,a}{2W\sqrt{1+2\varepsilon_m^W c}}, \tag{5}$$

where, f_m^L and f_m^W are the resonance frequency of the longitudinal and transverse mode, m is the oscillation mode, ε_m^L and ε_m^W are the constants which depends on the crack aspect ratio, W/L, and C is the crack stiffness that is given by

$$C = \left(\frac{2(1-\upsilon)}{1-2\nu}\right)\left(\frac{a}{\alpha}\right)^2\left(\frac{\rho_f}{\rho_s}\right)\left(\frac{L}{d}\right). \tag{6}$$

Here, υ is the Poisson ratio of the solid. We use the values for α = 3814 m s^{-1}, a = 1500 m s^{-1}, ρ_f = 1000 kg m^{-3}, ρ_s = 2627 kg m^{-3}, L = 30 cm and d = 0.2 cm to calculate the theoretical modes (see Table 1) and compare it with the observed modes. The values of ε_m^L & ε_m^W were calculated using the equations below considering γ as 0.22

$$\varepsilon_m^W = \begin{cases} (2/9m(mW/4\gamma L)^{1/2} & (W/L < 4\gamma/m) \\ (1/3m)(1-4\gamma L/3mW) & 4\gamma/m < W/L < 1 \end{cases} \tag{7}$$

$$\varepsilon_m^W = \left(W/L\right)\left(1/3m\right)\left(1-4\gamma L/3mL\right). \tag{8}$$

The experimental values of the frequencies have been presented in Table 2 along with the theoretical values. We calculate the percentage of the mismatch by

$$\text{mis} = (f_t - f_o)/f_t, \tag{9}$$

where f_t and f_o refer to the theoretical and observed values, respectively. The maximum mismatches between the theoretical and the observed frequencies is notable in the modes corresponding to the wavelength of 5 (*2 L/5*) for the longitudinal mode and 3 (*2 W/3*), where it is about 11 per cent. The value of the first mixed mode was estimated from Liang *et al.* (2024) and the value estimated from their numerical simulation is approximately 2850 Hz and our experimental observation is around 2830 Hz, with a misfit of 0.7 per cent. The frequency mismatch between the theoretical

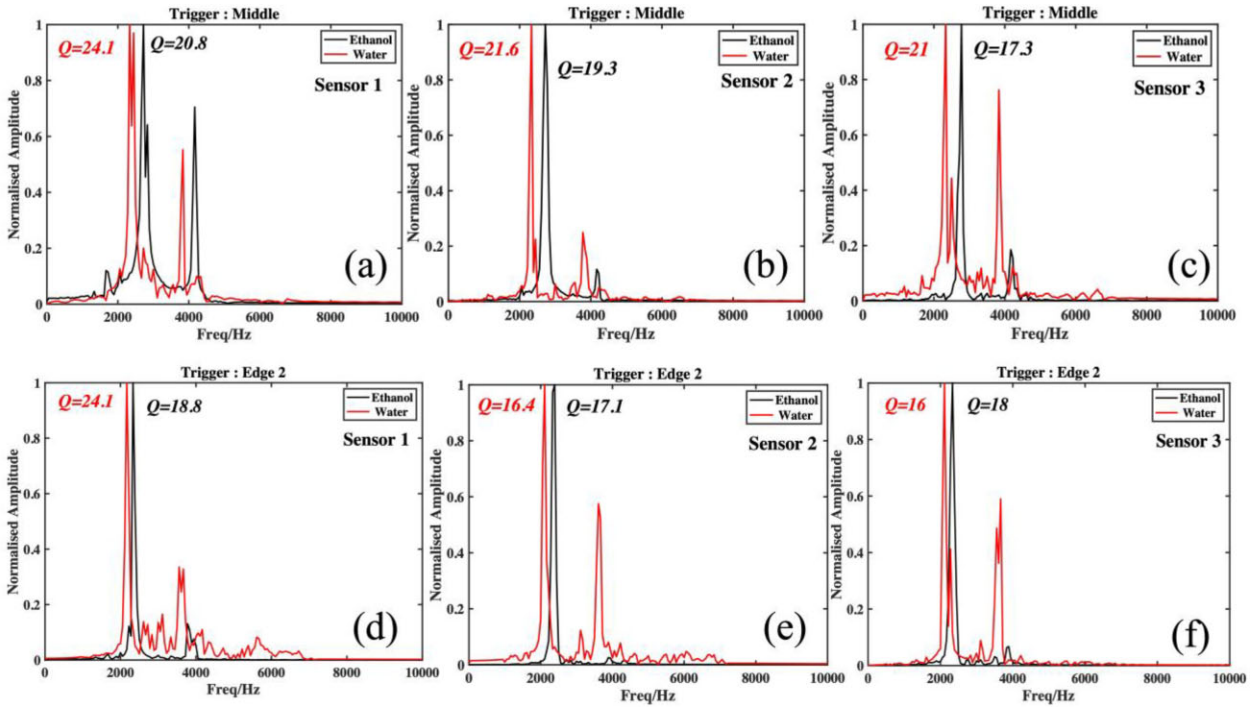

Figure 8. The amplitude spectrum contrast for the fluids ethanol and water with different sensor sites but the same middle trigger position is shown in panels (a)–(d). The amplitude spectrum contrast for the fluids ethanol and water with different sensor sites but the edge 2 trigger position is shown in panels (e)–(h).

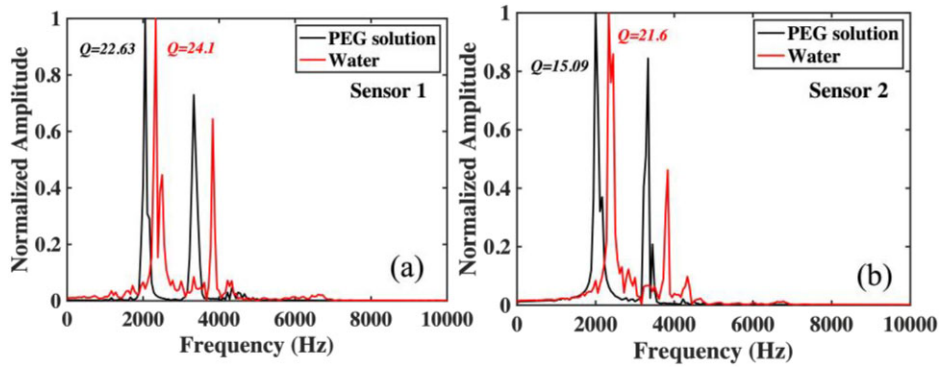

Figure 9. Quality factor and amplitude spectrum obtained for the PEG solution. Here, panels (a) & (b) represent the data obtained using a trigger location at the middle for Sensors 1 & 2

and experimentally observed longitudinal modes can be explained by 1-D approximation of the physical model, while the theoretical calculations were performed using a 2-D equation. Thus, in general, we note a satisfactory agreement between our observations and the theoretical values.

5.2 Limitation of the physical model

While there are distinct advantages to laboratory experiments that allow for more realistic modelling, there are some limitations of the apparatus that can complicate interpretations. The small mismatches between the values of the theoretical and experimental frequency for the higher modes may be partly explained by the relatively high source frequency used in our experiment. Cao *et al.* (2021) showed from the experimental characterization of Krauklis waves, that source frequency used in the experiment plays an important role in mode excitation. They used a 1000 Hz source frequency and were unable to excite fundamental modes or a few higher modes for 2.5 mm aperture crack model. In our physical model, we used a source frequency of 3000 Hz throughout the experiment, which restricted us from exciting the lower fundamental longitudinal mode and higher transverse and mixed modes; as a result, most of the modal energies we measured are near the source frequency.

Traditionally, a step pressure change on the surface of the crack model is used in theoretical and numerical studies (Chouet 1986, 1988). However, in our physical model, the source was placed on top of the concrete surface, connected to the crack, and was oscillatory in nature because burying a source near the crack surface would have restricted the repeatability and complete control of the source. This setup likely introduced distortion into the waveforms, preventing them from exhibiting a clean decay.

Finally, although the vertical tubes connected to the crack model could induce pressure loss, they were plugged tightly during the experiment. While the effect of these tubes appears to be minor, they may explain some of the discrepancy between theoretical and measured spectral values.

To improve alignment with theoretical predictions, future experiments could use lower source frequencies and alternative excitation techniques to better capture a broader range of modal energies. Enhanced source placement strategies (in direct contact of the crack model) might also mitigate waveform distortions and lead to clearer decay patterns, offering more accurate insights into the dynamic behaviour of crack models.

We use several approaches to demonstrate that the finite size of the concrete block does not influence the measured resonance frequencies. First, we estimated the fundamental in-plane and thickness resonance modes of the 3 m × 3 m × 0.24 m block using Mindlin–Reissner plate theory (also called first-order shear deformation theory for plates) (Reissner 1945; Mindlin 1951) for moderately thick structures. Detailed calculations are presented in Appendix C with the calculated values mentioned in Table A1. (eq. A4). We find that there is some overlap in the range of frequencies in some of the higher modes calculated for the concrete slab, but there are no frequencies that match our observations. Secondly, we have compared the frequency values obtained from exciting the crack both before and after embedding it into the bigger slab and confirm that they show the similar peaks. The frequency spectrum comparisons for the pressure transducers (before and after) are presented in Fig. S6 (Supporting Information). To clarify the observed second transverse mode, we present the amplitude spectrum obtained with a higher source frequency (5000 Hz) during the smaller slab's preliminary testing (Fig. S6b, Supporting Information). As, it matches the specified value range following embedment. We also note that if the observed resonance frequencies were overshadowed by the resonance of the concrete block, there should not been any changes in resonance frequency with the involvement of fluid density or viscosity as well, which are clearly observed in Figs 8 and 9. Finally, we note that we used a dynamic pressure transducer in close contact with the crack fluid to verify our observed results through the surface sensor. The transducer model used in our experiment is designed to record the fluid pressure and is relatively insensitive to vibration in the solid, so the frequencies obtained using the pressure transducer (which matches the surface sensors) are attributed to the frequencies corresponding to the crack wave resonance.

5.3 Our physical model and field observations

Laboratory-scale data can be linked to field-scale observations through either dimensionless numbers or scaling factors, both of which have been widely used in volcano seismology (Kavanagh *et al.* 2018). Here, we employ a formulation proposed by Burlini *et al.* (2007) to scale our lab data. According to Burlini *et al.* (2009), the frequency (f_n) and crack length (L_n) from natural LP events can be connected to those from lab-scale data (f_l and L_l) by

$$L_n \times f_n = L_l \times f_l, \tag{10}$$

where subscripts n and l denote natural and laboratory, respectively. For example, the lowest and highest observed longitudinal frequencies (values shown in Table 2) were 2166 and 4556 Hz. Our crack model has a L/d ratio of 150 and a stiffness of 22.8. Given the bulk modulus of a water steam in a hydrothermal system as 200 MPa and the rigidity of the volcanic rock matrix with a value of 10 GPa (Heap *et al.* 2020), the same stiffness in a natural setting will have a length to aperture ratio of 1140 (crack length of 130 m and an aperture of 0.114 m). Under such circumstances, the corresponding frequency can be observed around 4.8 Hz (using eq. 10). If we use the theoretical value of the fundamental frequency of our experimental crack model which is 1097 Hz, the observered frequency would be 2.5 Hz. Waite *et al.* (2008) found a dominant frequency of 1.7 Hz for the long-period waves in their analysis of the eruption dynamics at Mount St. Helens, and Kumagai *et al.* (2005) reported a dominant frequency of 1.3 Hz when elucidating the source mechanism of the LP events in Kilauea. We used the second longitudinal mode for the calculation, which resulted in a higher observed value.

In terms of the quality factor, from Table 1, we can note that the value of quality factor varies from 5 to 25 for all the trigger locations. Taguchi *et al.* (2021) calculated a wide range of quality factor values with varied width to length ratio along with varying α/a ratios. Our crack model has a W/L ratio of 0.5 and an α/a ratio of 2.6. According to that model, the quality factor values corresponding to the third longitudinal value for a crack similar to our model should have a range from 5 to 50, which agrees well with our observation. Field observations show that the quality factor can have a wide range of values from the 10 s to the 100 s and sometimes up to 500. In a study of the source mechanism of the Kusatsu–Shirane volcano, Japan by Nakano et al (2003), a Q value varied from 29–63 corresponding to a characteristic frequency of 1.27 Hz was reported. Experimental observations by Cao *et al.* (2021) indicate that the quality factor value for water as the fluid, with a crack aperture of 2.5 mm, falls within the range of 20 s.

Additionally, we have noted that our findings are qualitatively consistent with field observation. For instance, in a study of the eruption dynamics at Mount St. Helens, Waite *et al.* (2008) noted a subtle change in LP signals recorded closer to the vent. Since changes in the triggering mechanism can create stronger resonance in higher modes (Chouet and Matoza 2013), Waite *et al.* (2008) concluded that there was a possible temporal or spatial change in the triggering mechanism. This field observation aligns with the findings from our physical model, which demonstrated that the resonance frequency varies depending on the location of the trigger.

6. CONCLUSION

We developed a laboratory-scale physical model to investigate fundamental factors impacting LP seismic signals. Unlike previous experimental studies on LP seismicity, our physical model uses a controlled source, allowing for quantitative analysis of LP events with respect to available analytical or numerical models (e.g. Chouet's model). Thus, possible verifications or modifications of those models is feasible.

According to our results: (1) the data collected from the pressure transducer within the crack model shows a frequency spectrum similar to that obtained from surface sensors, which indicates that the surface sensors record the response of the crack; (2) trigger locations at the middle of the crack length and width effectively resonated the first and second transverse modes; (3) the quality factor decreases with increasing sensor distance from the crack; (4) the values of observed resonance frequencies of the LP waves are independent of the sensor locations; (5) by decreasing and increasing the fluid density, the resonance frequency increases and decreases respectively, while the quality factor decreases with increased density; and (6) with a controlled source and increasing fluid viscosity, both the resonance frequency and the quality factor decrease.

The proposed physical model will allow for considering more complex scenarios pertinent to cracks and fluids involved, such as various crack shapes, crack networks with and without connectivity, crack roughness, multiphase fluids, etc. Thus, our proposed physical

model will pave the way to achieve a profound understanding of LP seismicity with respect to real scenarios observed in natural settings.

ACKNOWLEDGMENTS

We are grateful to Eric Dunham for excellent suggestions that have improved the paper. This work was supported by the National Science Foundation EAR grant 2021768.

SUPPORTING INFORMATION

Supplementary data are available at *GJI* online.

Figure S1. Waveforms related to different sensor locations varied with different trigger locations, where (a)–(d) represents waveforms for Sensors 1–4 corresponding to the trigger location at edge 1, (e)–(h) for trigger location at edge 2, (i)–(l) for trigger location at middle and (m)–(o) for trigger location at one fourth location.

Figure S2. Frequency comparison between the surface sensors and the pressure transducer, where (a)–(d) represents the normalized amplitude spectrum for Sensors 1–4 corresponding to the trigger location at edge 1, (e)–(h) for trigger location at edge 2, (i)–(l) for trigger location at middle and (m)–(o) for trigger location at one fourth location.

Figure S3. Quality factor calculation for different sensor and trigger locations

Figure S4. Quality factor calculation for the ethanol using Nelder–Mead Simplex method. (a)–(c) Q factor calculation for the trigger location middle for Sensors 1–3. (d)–(f) Q factor calculation for the Edge trigger location for Sensors 1–3.

Figure S5. Amplitude spectrum of the background noise recorded during the experiment.

Figure S6. (a) The comparison between the frequency spectrum before and after embedment of the smaller slab inside the bigger one. (b) Frequency spectrum obtained using a higher source frequency.

Figure S7. (a) Time-series of the source used in the experiment. (b) Frequency spectrum of the source with a frequency of 3000 Hz.

Please note: Oxford University Press is not responsible for the content or functionality of any supporting materials supplied by the authors. Any queries (other than missing material) should be directed to the corresponding author for the paper.

DATA AVAILABILITY

All the data set used in this research can be found in Ray (2025).

REFERENCES

Aggelis, G.D., 2011. Classification of cracking mode in concrete by acoustic emission parameters, *Mech. Res. Commun.,* **38**(3), 153–157.

Aki, K., Fehler, M. & Das, S., 1977. Source mechanism of volcanic tremor: fluid-driven crack models and their application to the 1963 Kilauea eruption, *J. Volc. Geotherm. Res.,* **2**.

Aoyama, H. & Takeo, M., 2001. Wave properties and focal mechanisms of N-type earthquakes at Asama volcano, *J. Volc. Geotherm. Res.,* **105**(1–2), 163–182.

Bean, C., De Barros, L., Lokmer, I., Métaxian, J.-P., O'Brien, G. & Murphy, S., 2014. Long-period seismicity in the shallow volcanic edifice formed from slow-rupture earthquakes, *Nat. Geosci.,* **7,** 71–75.

Benson, P.M., Vinciguerra, S., Nasseri, M.H.B. & Young, R.P., 2014. Laboratory simulations of fluid/gas induced micro-earthquakes: application to volcano seismology, *Front. Earth Sci.,* **2**.

Bourbie, T., Coussy, O. & Zinszner, B., 1987. *Acoustics of Porous Media,* Edition Technip, Paris.

Burlini, L., Toro, G.D. & Meredith, P., 2009. Seismic tremor in subduction zones: rock physics evidence, *Geophys. Res. Lett.,* **36,** L08305.

Burlini, L., Vinciguerra, S., Toro, G.D., Natale, G.D., Meredith, P. & Burg, J.P., 2007. Seismicity preceding volcanic eruptions: new experimental insights, *Geology,* **35**(2), 183–186.

Cao, H., Medici, E. & Askari, R., 2021. Physical modelling of fluid-filled cracks using the dynamic photoelasticity technique, *Geophysics,* **86**(1), T33–T43.

Cao, H., Medici, E.F., Waite, G.P. & Askari, R., 2020. Effect of geometry and fluid viscosity on dynamics of fluid-filled cracks: insights from analog experimental observations, *Earth Space Sci.,* **7,** e2020EA001333.

Cao, H., Nakagawa, S. & Askari, R., 2021. Laboratory measurements of the impact of crack and fluid properties on the propagation of Krauklis waves, *J. Geophys. Res. Solid Earth.,* **126,** e2020JB021593.

Chouet, B., 1986. Dynamics of a fluid-driven crack in three dimensions by the finite difference method, *J. geophys. Res.,* **91**(B14), 13 967–13 992.

Chouet, B., 1988. Resonance of a fluid-driven crack: radiation properties and implications for the source of long-period events and harmonic tremor, *J. geophys. Res.,* **93**(B5), 4375–4400.

Chouet, B., 1996. Long-period volcano seismicity: its source and use in eruption forecasting, *Nature,* **380,** 309–316.

Chouet, B. & Julian, B.R., 1985. Dynamics of an expanding fluid-filled crack, *J. geophys. Res.,* **90**(B13), 11 187–11 198.

Chouet, B. & Matoza, R.S., 2013. A multi-decadal view of seismic methods for detecting precursors of magma movement and eruption, *J. Volc. Geotherm. Res.,* **252,** 108–175.

Corona-Romero, P., Arciniega-Ceballos, A. & Sánchez-Sesma, F.J., 2012. Simulation of LP seismic signals modelling the fluid–rock dynamic interaction, *J. Volc. Geotherm. Res.,* **211–212,** 92–111.

Cruz, F.G. & Chouet, B.A., 1997. Long-period events, the most characteristic seismicity accompanying the emplacement and extrusion of a lava dome in Galeras Volcano, Colombia, in 1991, *J. Volc. Geotherm. Res.,* **77**(1–4), 121–158.

Derode, B., Guglielmi, Y., De Barros, L. & Cappa, F., 2015. Seismic responses to fluid pressure perturbations in a slipping fault, *Geophys. Res. Lett.,* **42,** 3197–3203.

Dunham, E.M. & Ogden, D.E., 2012. Guided waves along fluid-filled cracks in elastic solids and instability at high flow rates, *ASME J. Appl. Mech.,* **79**(3), 03 1020.

Fazio, M., Benson, P.M. & Vinciguerra, S., 2017. On the generation mechanisms of fluid-driven seismic signals related to volcano-tectonics, *Geophys. Res. Lett.,* **44,** 734–742.

Ferrazzini, V. & Aki, K., 1987. Slow waves trapped in a fluid-filled infinite crack: implication for volcanic tremor, *J. geophys. Res.,* **92**(B9), 9215–9223.

Fujita, E. & Ida, Y., 2003. Geometrical effects and low-attenuation resonance of volcanic fluid inclusions for the source mechanism of long-period earthquakes, *J. geophys. Res.,* **108,** 2118.

Fujita, E., Ida, Y. & Oikawa, J., 1995. Eigen oscillation of a fluid sphere and source mechanism of harmonic volcanic tremor, *J. Volc. Geotherm. Res.,* **69**(3–4), 365–378.

Haney, M.M., Buurman, H., Holtkamp, S. & McNutt, S.R., 2021. Monochromatic long-period seismicity prior to the 2012 earthquake swarm at Little Sitkin Volcano, Alaska, *Front. Earth Sci.,* **9,** 689 651.

Heap, M.J., Villeneuve, M., Albino, F., Farquharson, J.I., Brothelande, E., Amelung, F., Got, J. & Baud, P., 2020. Towards more realistic values of elastic moduli for volcano modelling, *J. Volc. Geotherm. Res.,* **390,** 106 684.

Hori, S., Fukao, Y., Kumazawa, M., Furumoto, M. & Yamamoto, A., 1989. A new method of spectral analysis and its application to the Earth's free oscillations: the "Sompi" method, *J. geophys. Res.,* **94**(B6), 7535–7553.

James, M.R., Lane, S.J. & Chouet, B.A., 2006. Gas slug ascent through changes in conduit diameter: laboratory insights into a volcano-seismic source process in low-viscosity magmas, *J. Geophys. Res. Solid Earth,* **111**(B5), B05201.

Kavanagh, J., Engwell, S. & Martin, S., 2018. A review of analogue and numerical modelling in volcanology, *Solid Earth,* **9,** 531–571.
Korneev, V.A., 2008. Slow waves in cracks filled with viscous fluid, *Geophysics,* **73**(1), N1–N7.
Krauklis, P., 1962. On some low-frequency vibrations of a liquid layer in an elastic medium, *J. Appl. Math. Mech.,* **26**(6), 1685–1692.
Kumagai, H. & Chouet, B.A., 1999. The complex frequencies of long-period seismic events as probes of fluid composition beneath volcanoes, *Geophys. J. Int.,* **138**(2, August), F7–F12.
Kumagai, H. & Chouet, B.A.., 2000. Acoustic properties of a crack containing magmatic or hydrothermal fluids, *Geophys. J. Int.,* **105**(B11), 25 493–25 512.
Kumagai, H. & Chouet, B.A., 2001. The dependence of acoustic properties of a crack on the resonance mode and geometry, *Geophys. Res. Lett.,* **28**(17), 3325–3328.
Kumagai, H., Chouet, B.A. & Dawson, P.B., 2005. Source process of a long-period event at Kilauea volcano, Hawaii, *Geophys. J. Int.,* **161**(1), 243–254.
Kumagai, H., Chouet, B.A. & Nakano, M., 2002. Waveform inversion of oscillatory signatures in long-period events beneath volcanoes, *J. geophys. Res.,* **107**(B11), 2301.
Kumazawa, M., Imanishi, Y., Fukao, Y., Furumoto, M. & Yamamoto, A., 1990. A theory of spectral analysis based on the characteristic property of a linear dynamic system, *Geophys. J. Int.,* **101**(3), 613–630.
Liang, C., Peng, J., Ampuero, J.-P., Shauer, N. & Dai, K., 2024. Resonances of fluid-filled cracks with complex geometry and application to very long period (VLP) seismic signals at Mayotte submarine volcano, *J. Geophys. Res. Solid Earth,* **129,** e2023JB027844.
Lipovsky, B.P. & Dunham, E.M., 2015. Vibrational modes of hydraulic cracks: inference of crack geometry from resonant frequencies and attenuation, *J. Geophys. Res. Solid Earth.,* **120**.
Maeda, Y. & Kumagai, H., 2013. An analytical formula for the longitudinal resonance frequencies of a fluid-filled crack, *Geophys. Res. Lett.,* **40**(19), 5108–5112.
Matoza, R.S., Garcés, M.A., Chouet, B.A., D'Auria, L., Hedlin, H., Groot-Hedlin, C. & Waite, G.P., 2009. The source of infrasound associated with long-period events at Mount St. Helens, *J. geophys. Res.,* **114,** B04305.
Mindlin, R.D., 1951. Influence of rotary inertia and shear on flexural motions of isotropic, elastic plates, *J. Appl. Mech.,* **18,** 31–38.
Molina, I., Kumagai, H., Pennec, J.L. & Hall, M., 2005. Three-dimensional *P*-wave velocity structure of Tungurahua Volcano, Ecuador, *J. Volc. Geotherm. Res.,* **147**(1–2), 144–156.
Nakano, M. & Kumagai, H., 2005. Response of a hydrothermal system to magmatic heat inferred from temporal variations in the complex frequencies of long-period events at Kusatsu–Shirane Volcano, Japan, *J. Volc. Geotherm. Res.,* **147**(3–4), 233–244.
Nakano, M., Kumagai, H. & Chouet, B., 2003. Source mechanism of long-period events at Kusatsu–Shirane Volcano, Japan, inferred from waveform inversion of the effective excitation functions, *J. Volc. Geotherm. Res.,* **122**(3–4), 149–164.
Nakano, M., Kumagai, H., Kumazawa, M., Yamaoka, K. & Chouet, B.A., 1998. The excitation and characteristic frequency of the long-period volcanic event: an approach based on an inhomogeneous autoregressive model of a linear dynamic system, *J. geophys. Res.,* **103**(B5), 10 031–10 046.
Namiki, A., Takahashi, M. & Tsutsui, R., 2019. A model experiment of crack induced long-period events: injection of pressurized gas into a viscoelastic rock analogue, *Geophys. Res. Lett.,* **46,** 11 906–11 914.
Ray, S., 2025. A controlled source physical model for long period seismic events [Data set]. In Geophysical Journal International, *Zenodo,* https://doi.org/10.5281/zenodo.15276918
Ray, S., Cao, H., Waite, G.P. & Askari, R., 2024. Possibility of fluid flow characterization via a geophysical signal: experimental study on the Krauklis wave under fluid flow, *J. Geophys. Res. Solid Earth,* **129,** e2024JB029229.
Reissner, E., 1945. The effect of transverse shear deformation on the bending of elastic plates, *J. Appl. Mech.,* **12,** A69–A77.
Syahbana, D.K., Caudron, C., Jousset, P., Lecocq, T., Camelbeeck, T., Bernard, A. & Surono., 2014. Fluid dynamics inside a "wet" volcano inferred from the complex frequencies of long-period (LP) events: an example from Papandayan volcano, West Java, Indonesia, during the 2011 seismic unrest, *J. Volc. Geotherm. Res.,* **280,** 76–89
Taguchi, K., Kumagai, H., Maeda, Y. & Torres, R., 2018. Source properties and triggering processes of long-period events beneath volcanoes inferred from an analytical formula for crack resonance frequencies, *J. geophys. Res.,* **123,** 7550–7565.
Taguchi, K., Kumagai, H., Maeda, Y. & Torres, R., 2021. Empirical formula for the quality factors of crack resonances and its application to the estimation of source properties of long-period seismic events at active volcanoes, *Geophys. J. Int.,* **224**(3), 2131–2148.
Tary, J.B., Van der Baan, M. & Eaton, D.W., 2014. Interpretation of resonance frequencies recorded during hydraulic fracturing treatments, *J. Geophys. Res. Solid Earth,* **119**(2), 1295–1315.
Waite, G.P., Chouet, B.A. & Dawson, P.B., 2008. Eruption dynamics at Mount St. Helens imaged from broad-band seismic waveforms: interaction of the shallow magmatic and hydrothermal systems, *J. geophys. Res.,* **113,** B02305.
White, J.E., 1983. *Underground Sound-Application of Seismic Waves,* Elsevier Science Publ. Co. https://doi.org/10.1190/1.9781560802471

APPENDIX A: CALCULATION OF THE TUBE WAVE PROPAGATION

The velocity of the tube wave can be written as below (White 1983):

$$V_T = \left(\rho\left(\frac{1}{B} + \frac{1}{Eh/2b}\right)\right)^{-1/2} \quad \text{(A1)}$$

Where, ρ is the fluid density, B is the bulk modulus of the fluid, E is the Young's modulus of the tube containing the fluid, h is the thickness of the tube and b is the inner radius of the tube. The tubes used during our experiments were flexible vinyl tubes with a Young's modulus of approximately 0.56 GPa, inner radius of 0.3 cm and a thickness of 0.1 cm. Using these parameters, the velocity of the tube wave generated will be 299 m s^{-1}.

Now, the tube or conduit which comes out of the concrete slab has a length of around 72 cm and the tube which is used to drain the fluids from the crack model, has a length of approximately 2 m. Using these values, the two-way traveltime of the tube wave will be approximately, 4.8 and 13.3 millisecond, respectively.

APPENDIX B: RELATION BETWEEN THE FLUID DENSITY AND THE RESONANCE FREQUENCY

If we consider the crack stiffness C is larger than 1 (C>>1), then the eqs (4) and (5) can be modified as below (Maeda &

Table A1. Resonance frequency values for the concrete slab.

Mode (m, n)	$f_{(m,n)}$ (Hz)
(1,1)	317
(2,1) = (1,2)	793
(2,2)	1268
(3,1) = (1,3)	1584
(3,2) = (2,3)	2060
(3,3)	2851
(4,1) = (1,4)	2694
(4,2) = (2,4)	3171
(4,3) = (3,4)	3964

Kumagai 2013):

$$f_m^L \approx \frac{(m-1)\,a}{2L\sqrt{2\varepsilon_m^L C}}, \tag{A2}$$

$$f_m^W \approx \frac{(m-1)\,a}{2W\sqrt{2\varepsilon_m^W C}}. \tag{A3}$$

Now, substituting the value of the stiffness (C) from the eq. (1), we can write that f_m^L *or* $f_m^W \propto (\frac{1}{\rho_f^{1/2}})$, where ρ_f is the fluid density. From this relation, we can notice that decrease in fluid density will lead to the increase in the characteristic resonance. The ethanol used in our experiment has a density of 789 kg m^{-3}. From the above relation between the frequencies and the density of the fluid, we can write the change in the frequency as $\Delta f \propto (\frac{1}{\Delta\rho})$. Given these considerations, our data should exhibit an approximate 6.8 per cent shift in frequency.

APPENDIX C: CALCULATION REGARDING THE FUNDAMENTAL FREQUENCIES OF CONCRETE SLAB

According to the Mindlin–Reissner (first-order shear deformation) theory (Reissner 1945; Mindlin 1951), the resonance frequencies of a moderately thick slab can be written using this equation below:

$$\omega_{(m,n)}^2 = \frac{\mathrm{D}}{\rho_s h}\left(\alpha_{(m,n)}\right)^2 + k_s \frac{G}{\rho_s}\alpha_{(m,n)} \tag{A4}$$

$\omega_{(m,n)}$ is the natural circular frequency for mode indices $m, n = 1, 2, 3.\ldots\ldots$

And

$$\alpha_{(m,n)} = \pi^2\left(\frac{m^2}{a^2} + \frac{n^2}{b^2}\right) \tag{A5}$$

$D = \frac{Eh^3}{12(1-\upsilon^2)}$ is the bending rigidity, ρ_s is the density of the slab, υ is the Poisson's ratio, $k_s \approx (5/6)$ for a rectangular cross-section. The frequency $f_{(m,n)}$ has been calculated using $\frac{\omega_{(m,n)}}{2\pi}$.